Detection/estimation of the modulus of a vector. Application to point-source detection in polarization data

F. Argüeso,[1]⋆ J. L. Sanz,[2,3] D. Herranz,[2] M. López-Caniego[4] and J. González-Nuevo[5]

[1]*Departamento de Matemáticas, Universidad de Oviedo, 33007, Oviedo, Spain*
[2]*Instituto de Física de Cantabria, CSIC-UC, Av. los Castros s/n, Santander, 39005, Spain*
[3]*CNR Istituto di Scienza e Tecnologie dell'Informazione, via G. Moruzzi 1, I-56124, Pisa, Italy*
[4]*Astrophysics Group, Cavendish Laboratory, J.J. Thomson Avenue, Cambridge CB3 0HE*
[5]*SISSA-I.S.A.S., via Beirut 4, I-34014 Trieste, Italy*

ABSTRACT

Given a set of images, whose pixel values can be considered as the components of a vector, it is interesting to estimate the modulus of such a vector in some localized areas corresponding to a compact signal. For instance, the detection/estimation of a polarized signal in compact sources immersed in a background is relevant in some fields like astrophysics. We develop two different techniques, one based on the Neyman–Pearson lemma, the Neyman–Pearson filter (NPF), and another based on pre-filtering before fusion, the filtered fusion (FF), to deal with the problem of detection of the source and estimation of the polarization given two or three images corresponding to the different components of polarization (two for linear polarization, three including circular polarization). For the case of linear polarization, we have performed numerical simulations on two-dimensional patches to test these filters following two different approaches (a blind and a non-blind detection), considering extragalactic point sources immersed in cosmic microwave background (CMB) and non-stationary noise with the conditions of the 70 GHz *Planck* channel. The FF outperforms the NPF, especially for low fluxes. We can detect with the FF extragalactic sources in a high noise zone with fluxes $\geq$(0.42, 0.36) Jy for (blind/non-blind) detection and in a low noise zone with fluxes $\geq$(0.22, 0.18) Jy for (blind/non-blind) detection with low errors in the estimated flux and position.

Key words: polarization – methods: data analysis – techniques: image processing – cosmic microwave background – radio continuum: galaxies.

1 INTRODUCTION

The detection and estimation of the intensity of compact objects (or small regions) embedded in a background plus instrumental noise is relevant in different contexts, for example astrophysics, cosmology, medicine, teledetection, radar, etc. Different techniques have proven useful in the literature. Some of the proposed techniques are frequentist, such as the standard matched filter (MF; Nailong 1992; Vikhlinin et al. 1995; Malik & Subramanian 1997; Tegmark & de Oliveira-Costa 1998; Sanz et al. 2001; Herranz et al. 2002b; Stewart 2006), the matched multifilter (or multifrequency filter, Herranz et al. 2002a, 2005) or the recently developed matched matrix filters (Herranz & Sanz 2008; Herranz et al. 2009) that correspond to scalar, vector or matrix filters, respectively. Other frequentist techniques include continuous wavelets like the standard Mexican Hat

(Vielva et al. 2001, 2003; Barnard et al. 2004; Sanz et al. 2006) and other members of its family (González-Nuevo et al. 2006) and, more generally, filters based on the Neyman–Pearson approach using the distribution of maxima (López-Caniego et al. 2005a,b). All of these filters have been used in the literature, in particular, for the detection and estimation of the intensity of point-like sources (i.e. extragalactic objects) in cosmic microwave background (CMB) maps. In addition, some of them have been applied to real data like those obtained by the *Wilkinson Microwave Anisotropy Probe* (*WMAP*) satellite (López-Caniego et al. 2007) and simulated data (López-Caniego et al. 2006; Leach et al. 2008) for the upcoming experiment on board the *Planck* satellite (Tauber 2005). Besides, Bayesian methods have also been recently developed (Hobson & McLachlan 2003; Carvalho, Rocha & Hobson 2009).

In some applications, it is important to measure not only the intensity of the light (signal) but also its polarization. An example is the study of CMB radiation. The polarization is given by the Stokes parameters Q, U, V, and the total intensity of polarization

⋆E-mail: argueso@uniovi.es

is $P \equiv (Q^2 + U^2 + V^2)^{1/2}$ (Kamionkowski, Kosowsky & Stebbins 1997). For linear polarization, the previous expression reduces to $P \equiv (Q^2 + U^2)^{1/2}$. In such cases, three or two images are added quadratically followed by a square root.

Let us consider the case of linear polarization. In this case, we have two images Q, U and different approaches can be used to deal with detection/estimation of point-like sources on these maps. On the one hand, one can try to get the polarization P directly on the P-map. In this approach, we will consider one filter, obtained through the Neyman–Pearson technique (NPF). On the other hand, we can operate with two matched filters, each one on Q and U followed by a quadratic fusion and square root. We will call this procedure filtered fusion (FF). It is clear that from a formal point of view, we are trying to ask which is the optimal way to find the modulus of a vector given the components. In the case, we have only the map of the modulus of a vector and the components are unknown, the FF cannot be applied and the only possibility is the NPF.

We will develop the methodology for the cases of a two-vector and a three-vector because of the possible interesting applications to the two-plane and three-space. We will show the results when using numerical simulations on flat patches that are relevant for the component separation of sources (linear-polarized extragalactic sources) in CMB maps.

In Section 2, we develop the methodology. In Section 3, we describe the numerical simulations done in order to test the previous techniques. In Section 4, we present the main results, and in Section 5 we give the main conclusions.

2 METHODOLOGY

2.1 Two-vector

To develop our methodology, we will assume that we have a compact source, located for simplicity at the centre of two images Q, U and characterized by amplitudes A_Q, A_U and a profile $\tau(\vec{x})$, immersed in noises $n_Q(\vec{x})$ and $n_U(\vec{x})$ that are Gaussian and independently distributed with zero mean and dispersions $\sigma_Q(\vec{x})$ and $\sigma_U(\vec{x})$. Again, for simplicity, we will consider that $\sigma_Q(\vec{x}) = \sigma_U(\vec{x}) = \sigma(\vec{x})$, a condition that is verified in most polarization detectors. In general, we will consider that the noise is non-stationary. We remark that the previous assumptions can be easily generalized to different profiles and different types of noise in the two images but we will not consider it in this paper. We will assume a linear model for the two images,

$$d_{Q,U}(\vec{x}) = A_{Q,U}\tau(\vec{x}) + n_{Q,U}(\vec{x}). \tag{1}$$

The P-map, $P(\vec{x}) \equiv [Q^2(\vec{x}) + U^2(\vec{x})]^{1/2}$, is characterized by a source at the centre of the image with amplitude $A \equiv (A_Q^2 + A_U^2)^{1/2}$ immersed in non-additive noise which is correlated with the signal.

2.1.1 Neyman–Pearson filter on the P-map

If the noise is distributed normally and independently, then at any point the integration over the polar angle leads to the two-dimensional Rayleigh distribution of P in absence of the source (Papoulis 1984),

$$f(P|0) = \frac{P}{\sigma^2}e^{-P^2/2\sigma^2}, \tag{2}$$

whereas if the source is present, with amplitude A, one obtains the Rice distribution (Rice 1954),

$$f(P|A) = \frac{P}{\sigma^2}e^{-(A^2+P^2)/2\sigma^2}I_o\left(A\frac{P}{\sigma^2}\right), \tag{3}$$

where I_o is the modified Bessel function of zero order. If our image is pixelized, the different data P_i, $i = 1, \ldots, n$, with n the number of pixels, will follow the two distributions

$$(H_0): f(P_i|0) = \prod_i \frac{P_i}{\sigma_i^2}e^{-\sum_i P_i^2/2\sigma_i^2} \tag{4}$$

$$(H_1): f(P_i|A) = \prod_i \frac{P_i}{\sigma_i^2}I_o\left(A\frac{P_i\tau_i}{\sigma_i^2}\right)e^{-\sum_i(A^2\tau_i^2+P_i^2)/2\sigma_i^2}, \tag{5}$$

being σ_i the value of σ in the ith pixel, H_0, H_1 the null hypothesis (absence of source) and the alternative (presence of source), respectively, and τ_i the profile at the ith pixel. The log-likelihood is defined by

$$l(A|P_i) = \log\frac{f(H_1)}{f(H_0)} = -A^2\sum_i\frac{\tau_i^2}{2\sigma_i^2} + \sum_i\log I_o\left(A\frac{P_i\tau_i}{\sigma_i^2}\right). \tag{6}$$

The maximum likelihood estimator of the amplitude, $\hat{A}$, is given by the solution of the equation

$$\hat{A}\sum_i\frac{\tau_i^2}{\sigma_i^2} = \sum_i y_i\frac{I_1(\hat{A}y_i)}{I_o(\hat{A}y_i)}, y_i \equiv \frac{P_i\tau_i}{\sigma_i^2}. \tag{7}$$

This equation can be interpreted as a non-linear filter operating on the data that we will call the NPF.

2.1.2 Filtered fusion

In this case, we use the same matched filter (MF) operating over the two images Q, U, respectively, as given by (Argüeso & Sanz 2008)

$$\Phi(\vec{x}) \propto \frac{\tau(\vec{x})}{\sigma^2(\vec{x})}. \tag{8}$$

Then, with the two filtered images Q_{MF}, U_{MF} we make the non-linear fusion $P \equiv (Q_{MF}^2 + U_{MF}^2)^{1/2}$ pixel by pixel.

2.2 Three-vector

Now, we will assume that we have a compact source at the centre of three images Q, U, V characterized by amplitudes A_Q, A_U, A_V and a profile $\tau(\vec{x})$ immersed in noise $n_{Q,U,V}(\vec{x})$ that is Gaussian and independently distributed with zero mean and dispersion $\sigma(\vec{x})$. In general, we will consider that the noise is non-stationary. We will assume a linear model for the three images

$$d_{Q,U,V}(\vec{x}) = A_{Q,U,V}\tau(\vec{x}) + n_{Q,U,V}(\vec{x}). \tag{9}$$

The P-map, $P(\vec{x}) \equiv [Q^2(\vec{x}) + U^2(\vec{x}) + V^2(\vec{x})]^{1/2}$, is characterized by a source at the centre of the image with amplitude $A \equiv (A_Q^2 + A_U^2 + A_V^2)^{1/2}$ immersed in non-additive noise correlated with the signal.

2.2.1 NPF on the P-map

If the noise is distributed normally and independently, then at any point the integration over the angles leads to the three-dimensional

Rayleigh distribution in absence of the source, also called the Maxwell–Boltzmann distribution in Physics,

$$f(P|0) = \left(\frac{2}{\pi}\right)^{1/2} \frac{P^2}{\sigma^3} e^{-P^2/2\sigma^2}, \tag{10}$$

whereas if the source is present, with amplitude A, one obtains the distribution

$$f(P|A) = \left(\frac{2}{\pi}\right)^{1/2} \frac{P}{\sigma A} e^{-(A^2+P^2)/2\sigma^2} \sinh\left(\frac{AP}{\sigma^2}\right). \tag{11}$$

If our image is pixelized, the different data P_i, $i = 1, \ldots, n$ follow the two distributions

$$(H_0): f(P_i|0) = \left(\frac{2}{\pi}\right)^{n/2} \prod_i \frac{P_i^2}{\sigma_i^3} e^{-\sum_i P_i^2/2\sigma_i^2} \tag{12}$$

$$(H_1): f(P_i|A) = \left(\frac{2}{\pi}\right)^{n/2} \prod_i \frac{P_i}{\sigma_i A \tau_i}$$
$$\times \sinh\left(A\frac{P_i\tau_i}{\sigma_i^2}\right) e^{-\sum_i (A^2\tau_i^2+P_i^2)/2\sigma_i^2}, \tag{13}$$

being H_0, H_1 the null hypothesis (absence of source) and the alternative (presence of source), respectively, and τ_i the profile at the ith pixel. The log-likelihood is defined by

$$l(A|P_i) = \log \frac{f(H_1)}{f(H_0)} = -A^2 \sum_i \frac{\tau_i^2}{2\sigma_i^2}$$
$$- n \log A + \sum_i \log\left[\sinh\left(A\frac{P_i\tau_i}{\sigma_i^2}\right)\right]. \tag{14}$$

The maximum likelihood estimator of the amplitude, $\hat{A}$, is given by the solution of the equation

$$\hat{A} \sum_i \frac{\tau_i^2}{\sigma_i^2} + \frac{n}{\hat{A}} = \sum_i y_i \coth(\hat{A}y_i),\ y_i \equiv \frac{P_i\tau_i}{\sigma_i^2}. \tag{15}$$

This equation can be interpreted as a non-linear filter operating on the data that we will also call the NPF.

2.2.2 Filtered fusion

In this case, we use the same MF operating over the three images Q, U, V, respectively, as given by equation (8). Then, with the three filtered images Q_{MF}, U_{MF}, V_{MF}, we make the non-linear fusion $P \equiv (Q_{MF}^2 + U_{MF}^2 + V_{MF}^2)^{1/2}$ pixel by pixel.

3 SIMULATIONS

The European Space Agency *Planck* satellite (Tauber 2005), to be launched in 2009, will measure the anisotropies of the CMB with unprecedented accuracy and angular resolution. It will also analyse the polarization of this primordial light. It is of great interest the detection and estimation of polarized sources in CMB maps (Tucci et al. 2004, 2005; The Planck Collaboration 2006); since this radiation is linearly polarized (Kamionkowski et al. 1997), $V = 0$, we will apply the methods for the detection/estimation of the modulus of a two-vector presented in Section 2.1. However, some cosmological models predict a possible circular polarization of CMB radiation (see for example Cooray, Melchiorri & Silk 2003; Agarwal et al. 2008). Even if CMB is not circularly polarized, the extragalactic radio sources can indeed show circular polarization (Aller, Aller & Plotkin 2005; Homan et al. 2006; Kirk & Tsang 2006). Besides, circular polarization occurs in many other astrophysical areas, from

Solar Physics (Reiner et al. 2007; Tritschler et al. 2007) to interstellar medium (Cox et al. 2007), just to put a few examples. In all these cases, the results for the modulus of a three-vector presented in Section 2.2 could be useful.

In order to compare and evaluate the performance of the filters presented in Section 2.1, we have carried out two-dimensional simulations with the characteristics of the 70 GHz *Planck* channel (The Planck Collaboration 2006). The simulated images have 16×16 pixel with a pixel size of 3.43 arcmin. We simulate the Q and U components of the linear polarization as follows: each component consists of Gaussian uncorrelated detector noise plus the contribution of the CMB and a polarized point source filtered with a Gaussian-shaped beam whose full-width at half maximum (FWHM) is 14 arcmin (the FWHM of the 70 GHz *Planck* channel beam). So the source polarization components can be written as

$$s_Q \equiv A_Q \exp\left[-\frac{|\vec{x}|^2}{2\gamma^2}\right], \tag{16}$$

$$s_U \equiv A_U \exp\left[-\frac{|\vec{x}|^2}{2\gamma^2}\right], \tag{17}$$

where γ is the beam dispersion (size) and we assume that the source is centred at the origin. The CMB simulation is based on the observed *WMAP* low multipoles, and on a Gaussian realization assuming the *WMAP* best-fitting C_ℓ at high multipoles. We do not include other possible foregrounds, since we are doing a first approximation to the detection/estimation problem and we assume that we apply our filters to relatively clean areas far away enough from the Galactic plane. Alternatively, we could consider a case in which the majority of foregrounds have been previously removed by means of some component separation method.

We consider a realistic non-stationary detector noise. We have simulated the noise sky pattern for a *Planck* flight duration of 14 months, assuming a simple cycloidal scanning strategy with a 7° slow variation in the Ecliptic collatitude of the z-axis. This scanning strategy implies that the sky will be covered inhomogeneously. The simulations have the same characteristics as the ones used in Argüeso et al. (2006). In order to illustrate the effects of non-stationary noise, we have chosen two representative zones of the sky: one zone of high noise but quite isotropic and another zone of low noise but more anisotropic. The first zone is located in a region far from the Ecliptic poles, where the noise pattern is quite uniform and the number of hits per pixel of the detector is small. The average rms deviation of the first zone (high noise) in units of $\Delta T/T$ (thermodynamic) is $\sigma = 3 \times 10^{-5}$ (for each component Q and U) and its standard deviation is 4.2×10^{-6}. For this particular scanning strategy approximately 25 per cent of the sky has this kind of noise pattern. The second zone is close to one of the Ecliptic poles, where the sky is scanned more times (low noise level) but the hit pattern is very inhomogeneous. It has an average rms deviation $\sigma = 1.1 \times 10^{-5}$ and its standard deviation is 3.8×10^{-6}. Then, in the second zone the noise is lower but proportionally more anisotropic. For this scanning strategy, ~6 per cent of the sky has a noise pattern with these characteristics. Other zones of the sky would be intermediate cases between those considered here.

We take values of the source fluxes (before filtering with the Gaussian beam) F_Q and F_U ranging from 0.1 to 0.5 Jy with a step of 0.1 Jy. A flux of 0.1 Jy corresponds for the 70 GHz channel to $\Delta T/T = 1.9 \times 10^{-5}$, so that it is of the order of the detector noise rms deviation. The fluxes also correspond to typical polarization fluxes (Tucci et al. 2004; Tucci et al. 2005). As we will see in Section 4, for some low-noise cases, it is necessary to simulate

even lower flux sources in order to study the behaviour of the filters in the low signal-to-noise ratio regime. We will explicitly report on this in the appropriate cases in Section 4. The number of simulations is 500 for each combination of pairs of values of F_Q and F_U. After carrying out the corresponding simulations for Q and U, we add them quadratically and take the square root to calculate $P = \sqrt{Q^2 + U^2}$, the polarization modulus.

We study two different detection types: blind detection and non-blind detection. In the former case, we assume that we do not know the position of the source and then we place it at random in the image, in the latter case we know the source position and then we place it at the centre of the patch. We have considered images of 16×16 pixels in order to do fast calculations. In order to avoid border effects, we simulate and filter 24×24 pixel patches and, after the filtering step, we retain only the 16×16 pixel central square. We have tested the case of larger patches but the obtained results do not change significantly.

We use two different filters: the FF, which consists in the application of the MF to the images in Q and U separately in a first moment, and then the calculation/construction of P from the matched-filtered images Q_{MF} and U_{MF} and the NPF, applied directly on P, derived from the Neyman–Pearson lemma and presented with detail in Section 2. These filters are suitable for the case of uncorrelated noise, but we apply them to simulations including the CMB, which is correlated. However, we have checked that our results are similar when we consider simulations with and without the CMB: the relative differences of the errors in the estimated fluxes and positions are at most of a few per cent. This is due to the low value of the CMB rms deviation $\sigma \simeq 6 \times 10^{-7}$ as compared to that of the detector noise. Hence, the methods derived in Section 2.1 are also suitable for simulations including the CMB in the 70 GHz *Planck* case we consider.

In the blind case, we apply these filters to each simulation, centring the filters successively at each pixel, since we do not know the source position. We estimate the source amplitude A for the NPF, in this case, we calculate the value of A which maximizes the log-likelihood, equations (6) and (7). For the FF, we estimate separately A_Q and A_U and obtain $A = \sqrt{A_Q^2 + A_U^2}$.

We compute the absolute maximum of A in each filtered map and keep this value as the estimated value of the polarization P of the source and the position of the maximum as the position of the source. Note that in the more realistic case where more than one source can be present in the images, it is still possible to proceed as described by looking for local peaks in the image. In the non-blind case, we only centre the filters in the pixels included in one FWHM of the source centre (approximately 10 per cent of the total). In this way, we use the knowledge of the source position, then we calculate the absolute maximum of the estimated A in these pixels. We also calculate the significance level of each detection. In order to do this, we carry out 1000 simulations with $A_Q = 0$ and $A_U = 0$, and we calculate the estimated value of the source polarization in this case for each filter. We consider the null hypothesis, H_0, there is no polarized source, against the alternative hypothesis, H_1, there is a polarized source. We set a significance level $\alpha = 0.05$, this means that we reject the null hypothesis when a simulation has an estimated source amplitude higher than that of 95 per cent of the simulations without polarized source. We define the power of the test as $1 - \delta$, with δ the probability of accepting the null hypothesis when it is false, i.e. the power is the proportion of simulations with polarized source with an estimated amplitude higher than that of 95 per cent of the simulations without source.

The higher the power the more efficient the filter is for detection. Note that the test can be performed in the same way in the blind and non-blind cases: in the second case, we know the position of the source, but we do not know whether it is polarized or not.

4 RESULTS

4.1 Blind case

We carry out simulations in the blind case for the high noise and low noise zones as explained above. We apply the filters to the images and calculate the absolute maximum of A for each filtered
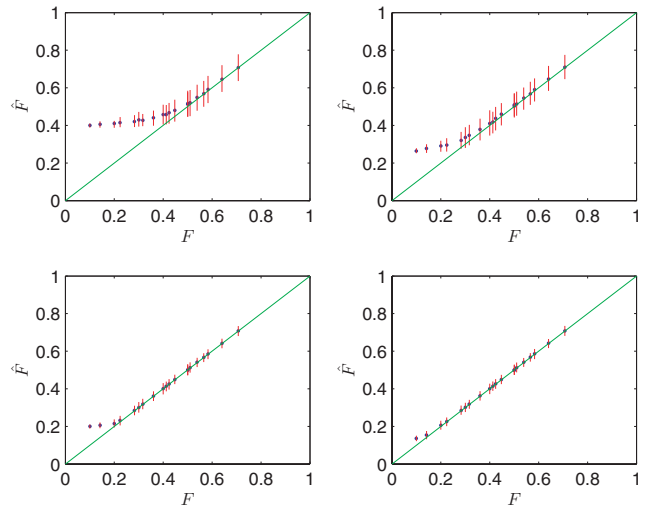

Figure 1. Blind detection. estimated flux $\hat{F}$ in Jy of the polarized sources plotted against their real flux F. The average and 68 per cent confidence intervals (vertical bar) of 500 simulations are plotted. Top left: the NPF has been used and the noise corresponds to the high-noise zone. Top right: FF and high noise. Bottom left: NPF and low noise. Bottom right: FF and low noise. In all the plots, the straight line $\hat{F} = F$ is drawn for comparison.
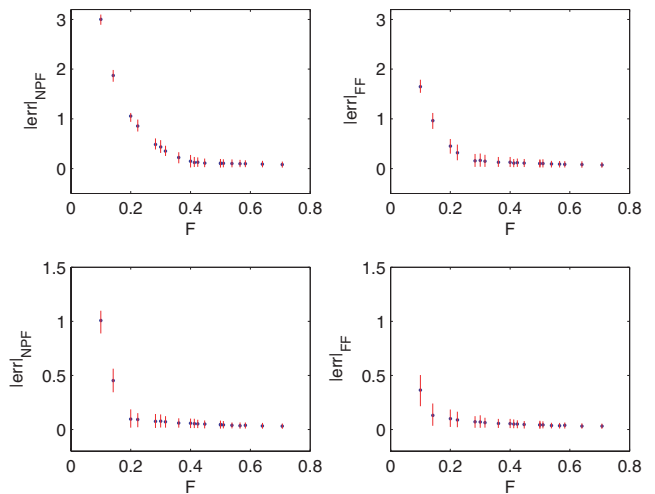

Figure 2. Blind detection. absolute value of the relative error, |err|, in the estimation of the flux of polarized sources plotted against the real flux F in Jy. The average and 68 per cent confidence intervals (vertical bar) of 500 simulations are plotted. Top left: the NPF is used with high noise. Top right: FF and high noise. Bottom left: NPF and low noise. Bottom right: FF and low noise.

image. If the detection has a significance higher than $\alpha = 0.05$, we consider it as a real detection, otherwise it would be a spurious one. For this significance level, we calculate the power of the detection test for the different pairs of F_Q and F_U values. We also calculate the estimated value of the polarization amplitude $\hat{A}$, convert it to the estimated flux in Jy, $\hat{F}$, and compare it with the real value $F = \sqrt{F_Q^2 + F_U^2}$. We plot $\hat{F}$ against F for the NPF and the FF with high and low noise in Fig. 1. We also compute the relative error of this estimation and its absolute value. For each pair of F_Q and F_U values, we obtain the average and 68 per cent confidence intervals of the absolute value of the relative error, taking into account the 500 performed simulations. These values are plotted against F in Fig. 2 for the same cases shown in Fig. 1. We also calculate the estimated position of the detected source and obtain the position error expressed in terms of the number of pixels. The power and the average of the relative error in F, of its absolute value and of the position error are presented in Table 1 for the two different types of noise. The rows in the table are sorted in ascending order of F. For the high noise case, we see in the table that the power for the FF is higher than for the NPF. The position and polarization errors

are also lower for the FF, this can also be seen in Figs 1 and 2. For $F > 0.6$ Jy, the FF and NPF perform similarly. For fluxes higher than 0.42 Jy, the power with the FF is $= 100$ per cent, the average relative error (bias) is ≤ 0.03, the average of the absolute value of the relative error is ≤ 0.12 and the average position error is ≤ 0.36. From now on, we will use the flux limit for which the power is 100 per cent as a measure of the filter performance.

The results for the low noise case are logically much better, the FF also performs better than the NPF. The power of the two filters quickly reaches 100 per cent for fluxes $F > 0.28$ Jy and the errors in both flux and position remain stable from fluxes $F \geq 0.40$ Jy. We therefore have cut the table at $F = 0.40$ Jy. In order to have a better sampling of the interesting signal-to-noise regime, we have simulated (using the same number of simulations as in the other cases) in addition the flux pairs $(F_Q, F_U) = (0.05, 0.10), (0.00, 0.15), (0.05, 0.15), (0.10, 0.15)$ and $(0.00, 0.25)$ Jy. This way the table is much more informative. For fluxes higher than 0.22 Jy, the power with the FF is 100 per cent, the average bias is ≤ 0.01, the average of the absolute value of the relative error is ≤ 0.09 and the average position error is ≤ 0.21.

Table 1. Blind detection. First column: pairs of values of F_Q and F_U in Jy and the corresponding value of F for the high-noise zone (top) and the low-noise zone (bottom). Second and third columns: detection power for the NPF and FF (percentage). Fourth and fifth columns: flux relative errors (average from 500 simulations) for the two filters. Sixth and seventh columns: absolute value of the relative error (average from 500 simulations). Eighth and ninth columns: position errors in numbers of pixels (average from 500 simulations).

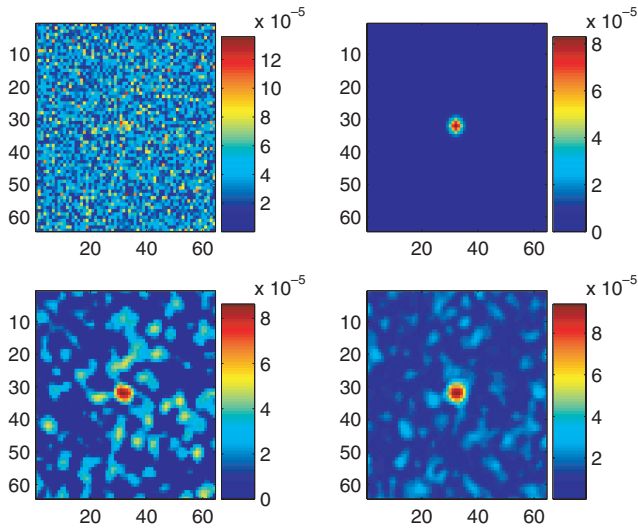| High noise ($F_Q, F_U : F$)	pow$_{NPF}$	pow$_{FF}$	err$_{NPF}$	err$_{FF}$	|err|$_{NPF}$	|err|$_{FF}$	pos$_{NPF}$	pos$_{FF}$
(0.00, 0.10; 0.10)	5	9	3.00	1.65	3.00	1.65	7.84	4.31
(0.10, 0.10; 0.14)	8	17	1.87	0.97	1.87	0.97	7.97	2.74
(0.00, 0.20; 0.20)	9	43	1.06	0.45	1.06	0.45	4.57	1.47
(0.10, 0.20; 0.22)	13	54	0.86	0.32	0.86	0.32	4.40	1.13
(0.20, 0.20; 0.28)	22	81	0.48	0.13	0.48	0.16	2.32	0.88
(0.00, 0.30; 0.30)	29	91	0.43	0.12	0.43	0.16	1.73	0.73
(0.10, 0.30; 0.32)	37	94	0.35	0.10	0.35	0.15	2.23	0.63
(0.20, 0.30; 0.36)	52	99	0.22	0.05	0.22	0.13	1.26	0.48
(0.00, 0.40; 0.40)	64	99	0.14	0.02	0.15	0.13	1.11	0.46
(0.10, 0.40; 0.41)	73	99	0.11	0.01	0.12	0.11	1.18	0.40
(0.30, 0.30; 0.42)	78	100	0.10	0.03	0.13	0.12	0.92	0.36
(0.20, 0.40; 0.45)	87	100	0.07	0.03	0.11	0.11	0.97	0.28
(0.00, 0.50; 0.50)	93	100	0.02	0.01	0.10	0.10	0.59	0.28
(0.30, 0.40; 0.50)	97	100	0.03	0.02	0.11	0.10	0.67	0.29
(0.10, 0.50; 0.51)	95	100	0.02	0.01	0.11	0.10	0.58	0.27
(0.20, 0.50; 0.54)	98	100	0.02	0.01	0.10	0.09	0.51	0.17
(0.40, 0.40; 0.57)	99	100	0.01	0.00	0.10	0.09	0.39	0.17
(0.30, 0.50; 0.58)	100	100	0.01	0.01	0.10	0.09	0.41	0.19
(0.40, 0.50; 0.64)	100	100	0.01	0.01	0.09	0.08	0.27	0.10
(0.50, 0.50; 0.71)	100	100	0.00	0.00	0.08	0.07	0.20	0.10
Low noise ($F_Q, F_U : F$)	pow$_{NPF}$	pow$_{FF}$	err$_{NPF}$	err$_{FF}$	|err|$_{NPF}$	|err|$_{FF}$	pos$_{NPF}$	pos$_{FF}$
(0.00, 0.10; 0.10)	5	39	1.01	0.37	1.01	0.37	4.53	1.57
(0.05, 0.10; 0.11)	9	53	0.81	0.23	0.81	0.23	5.04	1.16
(0.10, 0.10; 0.14)	17	91	0.45	0.08	0.45	0.13	2.54	0.55
(0.00, 0.15; 0.15)	19	93	0.39	0.07	0.39	0.13	1.94	0.48
(0.05, 0.15; 0.16)	27	97	0.32	0.05	0.32	0.13	2.13	0.45
(0.10, 0.15; 0.18)	55	99	0.16	0.03	0.16	0.12	1.30	0.34
(0.00, 0.20; 0.20)	79	99	0.08	0.03	0.10	0.10	0.71	0.24
(0.10, 0.20; 0.22)	92	100	0.04	0.01	0.09	0.09	0.45	0.21
(0.00, 0.25; 0.25)	99	100	0.00	0.00	0.08	0.08	0.43	0.16
(0.20, 0.20; 0.28)	100	100	0.01	0.01	0.08	0.07	0.18	0.09
(0.00, 0.30; 0.30)	100	100	0.00	0.00	0.08	0.07	0.20	0.10
(0.10, 0.30; 0.32)	100	100	0.01	0.01	0.07	0.06	0.15	0.08
(0.20, 0.30; 0.36)	100	100	0.00	0.00	0.06	0.06	0.10	0.05
(0.00, 0.40; 0.40)	100	100	0.00	0.00	0.06	0.05	0.05	0.03

Figure 3. Blind detection image. Top left: image of a polarized source filtered with a Gaussian beam (FWHM = 14 arcmin) placed in the centre of an image of 64×64 pixels with pixel size = 3.43 arcmin. The source polarization flux components are $(F_Q, F_U) = (0.4, 0.4)$ in Jy and it is embedded in CMB plus detector noise (high-noise zone). Top right: the image of the polarized source only. Bottom left: the first image after the application of the NPF. Bottom right: the first image after the application of the FF.

The FF is also much faster than the NPF. For instance, the analysis of an image of 64×64 pixel in a personal computer takes 7 s with the FF and about 6 min with the NPF. This is due to the maximization involved. The computation time grows proportionally to the number of pixels, so that the NPF could be too slow if we want to analyse large images. This is the reason why we have considered small patches.

Finally, we show in Fig. 3, four images corresponding to a polarized source with $(F_Q, F_U) = (0.4, 0.4)$ embedded in high noise. For the sake of a better visualization, we show 64×64 pixel images instead of the 16×16 sized images used in the simulations. We show the original image in P including noise, CMB and source, the image of the source, the image filtered with the NPF and the image treated with the FF method. By simple visual inspection, it is possible to see that the FF performs better than the NPF.

4.2 Non-blind case

We carry out simulations with a polarized source placed in the image centre and filter the images with the two different filters, centring them in the pixels at a distance from the source less than one FWHM. We simulate the same range of (F_Q, F_U) pairs as in the blind case (Section 4.1). Then, as in the blind case, we calculate the maximum in A, using only the selected pixels. This maximum is the estimated polarization of the source $\hat{A}$ and the pixel where we find the maximum is the source position, we convert this amplitude to the estimated flux in Jy, $\hat{F}$. We have also performed a detection test, accepting as real sources only those detected with a significance lower than $\alpha = 0.05$. In Table 2, we write the power of the test, the average of the relative polarization error, of its absolute value and of the position error. Our results are obtained from 500 simulations for each combination of pairs (F_Q, F_U) with high and low noise. The detection power is higher for the FF than for the other filter. For the high noise case, the improvement is very clear for $F \leq 0.50$ Jy; we also obtain higher powers for the non-blind case than for the blind

one. This could be expected, since we know the source position in the former case.

The position and polarization errors are also lower for the FF, this can also be seen in Figs 4 and 5, which show the same quantities as Figs 1 and 2 for non-blind detection. For fluxes higher than 0.36 Jy, the power with the FF is 100 per cent, the bias is ≤ 0.03, the average of the absolute value of the relative error is ≤ 0.13 and the average position error is ≤ 0.55. The flux and position errors are lower in the non-blind case than in the blind one, especially, for low fluxes.

The results for the low-noise case are much better, the FF outperforms the NPF. From 0.28 Jy on the results are quite similar. For fluxes higher than 0.18 Jy, the power with the FF is 100 per cent, the average bias is ≤ 0.02, the average of the absolute value of the relative error is ≤ 0.11 and the average position error is ≤ 0.39. Similarly to what happened with the low-noise case of Table 1, we have cut the table at flux $F = 0.40$ Jy and we have added new cases in order to have a better sampling of the interesting signal-to-noise regime. In this case, we have simulated the pairs $(F_Q, F_U) = (0.05, 0.10), (0.00, 0.12), (0.00, 0.13), (0.00, 0.15), (0.10, 0.15)$ and $(0.00, 0.25)$ Jy. The non-blind case gives better results than the blind one, especially for low fluxes.

5 CONCLUSIONS

In this paper, we deal with the detection and estimation of the modulus of a vector, a problem of great interest in general and in particular in astrophysics when we consider the polarization of the CMB. The polarization intensity P is defined as $P \equiv (Q^2 + U^2 + V^2)^{1/2}$, where Q, U and V are the Stokes parameters. We consider the case of images in Q, U and V consisting of a compact source with a profile $\tau(\vec{x})$ immersed in Gaussian uncorrelated noise. We intend to detect the source and estimate its amplitude in P by using two different methods: a NPF operating in P and based on the maximization of the corresponding log-likelihood and a FF procedure, that is the application of the MF on the images of Q, U and V and the combination of the corresponding estimates by making the non-linear fusion $P \equiv (Q_{MF}^2 + U_{MF}^2 + V_{MF}^2)^{1/2}$. We present the two filters in Section 2 for two-dimensional, $V = 0$, and three-dimensional vectors, deriving the corresponding expressions for the estimation of the polarized source amplitude.

Since we are interested in applying these different filters to the CMB and this radiation is linearly polarized, we will only consider the two-dimensional vector case in our simulations.

Our goal is to compare the performance of the filters when applied to simulated images. Then, we carry out two-dimensional simulations with the characteristics of the 70 GHz *Planck* channel. The images have 16×16 pixels with a pixel size of 3.43 arcmin. We simulate the Q and U components consisting of a compact source filtered with a Gaussian-shaped beam (FWHM of 14 arcmin) plus CMB and non-stationary detector noise. We consider two typical zones of the *Planck* survey: one with high noise and quite isotropic and another one with low noise but proportionally more anisotropic. These zones are extreme cases for the assumed scanning strategy we have chosen, and any other zone of the sky is an intermediate case between these two.

We study two types of detection: blind detection, in which we do not know the source position and non-blind, in which the position is known; we place the source at the centre of the image. We take values of the source fluxes in Q and U, F_Q and F_U, ranging from 0.1 to 0.5 Jy with a step of 0.1 Jy. Note that for extragalactic objects both Q and U can take negative values, but since the sign of both components is irrelevant for the calculation of P here we only

Table 2. Non-blind detection. First column: pairs of values of F_Q and F_U in Jy and the corresponding value of F for the high-noise zone (top) and the low-noise zone (bottom). Second and third columns: detection power for the NPF and FF (percentage). Fourth and fifth columns: flux relative errors (average from 500 simulations) for the two filters. Sixth and seventh columns: absolute value of the relative error (average from 500 simulations). Eighth and ninth columns: position errors in numbers of pixels (average from 500 simulations).

High noise (F_Q, F_U : F)	pow_{NPF}	pow_{FF}	err_{NPF}	err_{FF}	$|err|_{NPF}$	$|err|_{FF}$	pos_{NPF}	pos_{FF}
(0.00, 0.10; 0.10)	9	19	2.53	1.33	2.53	1.33	1.90	1.52
(0.10, 0.10; 0.14)	13	35	1.52	0.74	1.52	0.74	1.70	1.37
(0.00, 0.20; 0.20)	22	68	0.84	0.32	0.84	0.32	1.53	1.09
(0.10, 0.20; 0.22)	32	78	0.66	0.23	0.66	0.24	1.44	0.90
(0.20, 0.20; 0.28)	52	95	0.35	0.10	0.35	0.17	1.26	0.81
(0.00, 0.30; 0.30)	53	99	0.28	0.06	0.28	0.16	1.18	0.67
(0.10, 0.30; 0.32)	63	98	0.26	0.07	0.26	0.15	1.13	0.66
(0.20, 0.30; 0.36)	77	100	0.14	0.03	0.16	0.13	0.92	0.55
(0.00, 0.40; 0.40)	90	100	0.08	0.03	0.14	0.13	0.79	0.38
(0.10, 0.40; 0.41)	92	100	0.06	0.02	0.13	0.12	0.77	0.39
(0.30, 0.30; 0.42)	94	100	0.06	0.03	0.13	0.12	0.77	0.39
(0.20, 0.40; 0.45)	97	100	0.04	0.02	0.12	0.11	0.72	0.40
(0.00, 0.50; 0.50)	99	100	0.02	0.02	0.11	0.10	0.58	0.25
(0.30, 0.40; 0.50)	100	100	0.02	0.02	0.11	0.10	0.59	0.29
(0.10, 0.50; 0.51)	99	100	0.02	0.01	0.11	0.09	0.59	0.30
(0.20, 0.50; 0.54)	100	100	0.02	0.02	0.11	0.09	0.49	0.22
(0.40, 0.40; 0.57)	100	100	0.01	0.00	0.10	0.09	0.40	0.18
(0.30, 0.50; 0.58)	100	100	0.01	0.01	0.10	0.09	0.43	0.16
(0.40, 0.50; 0.64)	100	100	0.01	0.01	0.09	0.08	0.30	0.14
(0.50, 0.50; 0.71)	100	100	0.01	0.01	0.08	0.08	0.23	0.11
Low noise (F_Q, F_U : F)	pow_{NPF}	pow_{FF}	err_{NPF}	err_{FF}	$|err|_{NPF}$	$|err|_{FF}$	pos_{NPF}	pos_{FF}
(0.00, 0.10; 0.10)	12	69	0.77	0.20	0.77	0.21	1.44	0.78
(0.05, 0.10; 0.11)	22	88	0.58	0.15	0.58	0.18	1.52	0.72
(0.00, 0.12; 0.12)	24	93	0.47	0.10	0.47	0.15	1.18	0.65
(0.00, 0.13; 0.13)	34	95	0.38	0.09	0.38	0.16	1.14	0.57
(0.10, 0.10; 0.14)	48	98	0.26	0.06	0.26	0.14	0.92	0.51
(0.00, 0.15; 0.15)	57	99	0.21	0.05	0.21	0.14	0.82	0.52
(0.10, 0.15; 0.18)	87	100	0.07	0.01	0.11	0.11	0.61	0.39
(0.00, 0.20; 0.20)	94	100	0.03	0.02	0.12	0.11	0.56	0.28
(0.10, 0.20; 0.22)	99	100	0.03	0.02	0.10	0.09	0.39	0.23
(0.00, 0.25; 0.25)	100	100	0.02	0.01	0.09	0.08	0.32	0.15
(0.20, 0.20; 0.28)	100	100	0.01	0.01	0.08	0.07	0.22	0.11
(0.00, 0.30; 0.30)	100	100	0.01	0.01	0.08	0.07	0.21	0.09
(0.10, 0.30; 0.32)	100	100	0.00	0.00	0.08	0.07	0.16	0.08
(0.20, 0.30; 0.36)	100	100	0.00	0.01	0.06	0.06	0.09	0.04
(0.00, 0.40; 0.40)	100	100	0.00	0.01	0.05	0.05	0.08	0.04

simulate the positive case. We carry out 500 simulations for each pair (F_Q, F_U) and for all the cases of blind and non-blind detection with high and low noise.

We apply the filters to the simulated images, estimating the source amplitude A as the maximum value of P in the filtered images and the source position as the position of this maximum, then we convert the source amplitude to the source flux in Jy . We fix a significance $\alpha = 0.05$ for the detection and calculate a detection power for this significance, see Section 3 for more details. We also calculate the relative error of the estimated flux, its absolute value and the position error (in number of pixels), these errors together with the detection power are written in Tables 1 and 2 for the blind and non-blind case. We also show the estimated fluxes and the absolute value of the relative errors in Figs 1, 2, 4 and 5 for the different cases.

The FF performs better than the NPF (as can be seen in the tables and figures), especially for low fluxes and it is also much faster than the NPF. However, NPF is still interesting in a case where only the modulus of a vector is known and not its components (e.g., if we had a map of P polarization but not the Q and U maps separately). The powers are much higher and the errors much lower for the low noise case than for the high noise one. The filters also perform better in the non-blind case than in the blind one, especially for low fluxes.

We can detect extragalactic point sources in polarization images (at 100 per cent power) with the FF in the high-noise zone with fluxes $\geq(0.42, 0.36)$ Jy for (blind/non-blind) detection and in the low noise zone with fluxes $\geq(0.22, 0.18)$ Jy for (blind/non-blind) detection. The bias and the position error are very low ≤ 0.03 and <1 pixel, respectively, for all these fluxes.
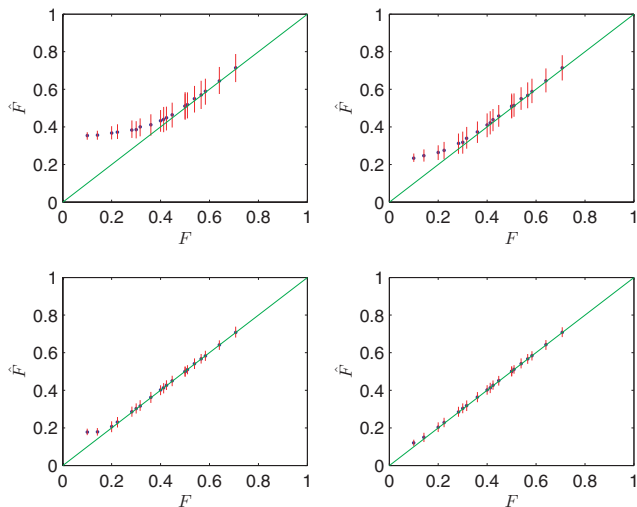
ACKNOWLEDGMENTS

Figure 4. Non-blind detection. Estimated flux of the polarized sources $\hat{F}$ in Jy plotted against their real flux F. The average and 68 per cent confidence intervals (vertical bar) of 500 simulations are plotted. Top left: the NPF has been used and the noise corresponds to the high noise zone. Top right: FF and high noise. Bottom left: NPF and low noise. Bottom right: FF and low noise. In all the plots the straight line $\hat{F} = F$ is drawn for comparison.
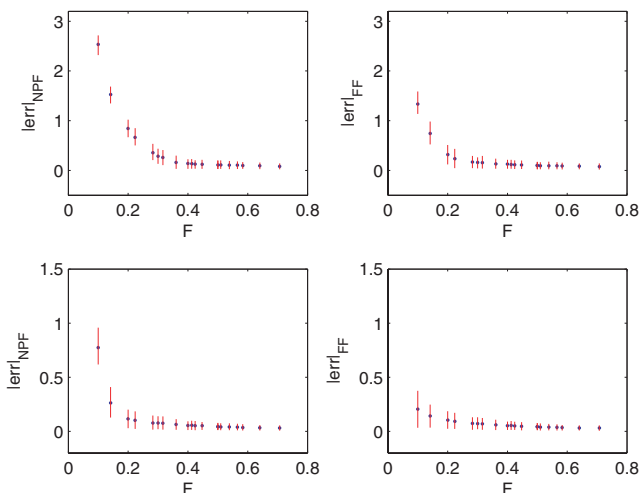

Figure 5. Non-blind detection. Absolute value of the relative error, |err|, in the estimation of the flux of polarized sources plotted against the real flux F in Jy. The average and 68 per cent confidence intervals (vertical bar) of 500 simulations are plotted. Top left: the NPF is used with high noise. Top right: FF and high noise. Bottom left: NPF and low noise. Bottom right: FF and low noise.

REFERENCES

Agarwal N., Jain P., McKay D. W., Ralston J. P., 2008, Phys. Rev. D, 78, 085028
Aller M. F., Aller H. D., Plotkin R. M., 2005, BAAS, 37, 1371
Argüeso F., Sanz J. L., 2008, in Reilly R., ed., Proc. 16th Eur. Signal Process. Conf., Filter Design for the Detection of Compact Sources Embedded in Non-Stationary Noise Plus a Deterministic Background. Lausanne, Switzerland, p. 1
Argüeso F., Sanz J. L., Barreiro R. B., Herranz D., González-Nuevo J., 2006, MNRAS, 373, 311
Barnard V. E., Vielva P., Pierce-Price D. P. I., Blain A. W., Barreiro R. B., Richer J. S., Qualtrough C., 2004, MNRAS, 352, 961
Carvalho P., Rocha G., Hobson M. P., 2009, MNRAS, 393, 681
Cooray A., Melchiorri A., Silk J., 2003, Phys. Lett. B, 554, 1
Cox N. L. J. et al., 2007, A&A, 465, 899
González-Nuevo J., Argüeso F., López-Caniego M., Toffolatti L., Sanz J. L., Vielva P., Herranz D., 2006, MNRAS, 369, 1603
Górski K. M., Hivon E., Banday A. J., Wandelt B. D., Hansen F. K., Reinecke M., Bartelmann M., 2005, ApJ, 622, 759
Herranz D., Sanz J. L., 2008, IEEE J. Sel. Topics in Signal Processing, 2(5), 727
Herranz D., Sanz J. L., Hobson M. P., Barreiro R. B., Diego J. M., Martínez-González E., Lasenby A. N., 2002a, MNRAS, 336, 1057
Herranz D., Gallegos J., Sanz J. L., Martínez-González E., 2002b, MNRAS, 334, 533
Herranz D., López-Caniego M., Sanz J. L., González-Nuevo J., 2009, MNRAS, 394, 510
Herranz D., Sanz J. L., Barreiro R. B., López-Caniego M., 2005, MNRAS, 356, 944
Hobson M. P., McLachlan C., 2003, MNRAS, 338, 765
Homan D. C., Lister M. L., Aller H. D., Aller M. F., Wardle J. F., 2006, BAAS, 38, 904
Kamionkowski M., Kosowsky A., Stebbins A., 1997, Phys. Rev. D, 55, 7368
Kirk J. G., Tsang O., 2006, A&A, 447, L13
Leach S. M. et al., 2008, A&A, 481, 597
López-Caniego M., Herranz D., Sanz J. L., Barreiro R. B., 2005a, EUSAIP Journal on Applied Signal Processing, 15, 2426
López-Caniego M., Herranz D., Barreiro R. B., Sanz J. L., 2005b, MNRAS, 359, 993
López-Caniego M., Herranz D., González-Nuevo J., Sanz J. L., Barreiro R. B., Vielva P., Argüeso F., Toffolatti L., 2006, MNRAS, 370, 2047
López-Caniego M., González-Nuevo J., Herranz D., Massardi M., Sanz J. L., De Zotti G., Toffolatti L., Argüeso F., 2007, ApJS, 170, 108
Malik R. K., Subramanian K., 1997, A&A, 317, 318
Nailong W., 1992, in Worrall D. M., Biemesderfer C., Barnes J., eds, ASP Conf. Ser. Vol. 25, Astronomical Data Analysis Software and Systems I. Astron. Soc. Pac., San Francisco, p. 291
Papoulis A., 1984, Probability, Random Variables, and Stochastic Processes. McGraw-Hill, New York
Reiner M. J., Fainberg J., Kaiser M. L., Bougeret J.-L., 2007, Sol. Phys., 241, 351
Rice S. O., 1954, Selected Papers on Noise and Stochastic Processes. Dover Pubns, p. 133
Sanz J. L., Herranz D., Martínez-González E., 2001, ApJ, 552, 484
Sanz J. L., Herranz D., López-Caniego M., Argüeso F., 2006, in Gini F., Kuruoglu E. E., eds, Proc. 14th EUSIPCO Conf., Wavelets on the Sphere. Application to the Detection Problem, eprint (astro-ph/0609351)
Stewart I. M., 2006, A&A, 454, 997
Tauber J. A., 2005, in Lasenby A. N., Wilkinson A., eds, Proc. IAU Symp. 201, New Cosmological Data and the Values of the Fundamental Parameters. Astron. Soc. Pac., San Francisco, p. 86
Tegmark M., de Oliveira-Costa A., 1998, ApJ, 500, L83
The Planck Collaboration, 2006, The Scientific Programme of Planck, ESA-SCI(2005-1) (astro-ph/0604069v1)
Tritschler A., Müller D. A. N., Schlichenmaier R., Hagenaar H. J., 2007, ApJ, 671, L85
Tucci M., Martínez-González E., Toffolatti L., González-Nuevo J., De Zotti G., 2004, MNRAS, 349, 1267
Tucci M., Martínez-González E., Vielva P., Delabrouille J., 2005, MNRAS, 360, 935
Vielva P., Barreiro R. B., Hobson M. P., Martínez-González E., Lasenby A. N., Sanz J. L., Toffolatti L., 2001, MNRAS, 328, 1
Vielva P., Martínez-González E., Gallegos J. E., Toffolatti L., Sanz J. L., 2003, MNRAS, 344, 89
Vikhlinin A., Forman W., Jones C., Murray S., 1995, ApJ, 451, 542

This paper has been typeset from a TEX/LATEX file prepared by the author.